Archive of Applied Mechanics
https://doi.org/10.1007/s00419-021-02034-9

ORIGINAL

**Martina Bukač** · **Shawn C. Shadden**

# Quantifying the effects of intraluminal thrombi and their poroelastic properties on abdominal aortic aneurysms

Received: 4 January 2021 / Accepted: 22 August 2021


**Abstract** We introduce a poroelastic model for intraluminal thrombus (ILT) that captures both the flow within ILT and its deformation. The model for ILT is coupled with blood flow and arterial wall deformation and used to study the biomechanics in image-based abdominal aortic aneurysm (AAA) models. Three different patient-specific geometries were considered in this study. Using finite element analysis, numerical simulations were performed to investigate the role of ILT on the risk of AAA rupture as assessed by Peak Wall Stress (PWS). Our results indicate that the presence of ILT may reduce wall stress in AAA. However, our results indicate that ILT permeability has little effect on AAA PWS, and that similar values of PWS are obtained with both porous and nonporous ILT models.

**Keywords** Abdominal aortic aneurysm · Intraluminal thrombus · Poroelasticity · Fluid–structure interaction · Multi-component model

## 1 Introduction

An abdominal aortic aneurysm (AAA) occurs when weakened aortic walls bulge or dilate. Because the aorta is the primary conduit of blood to the body, a ruptured AAA can cause life-threatening bleeding. Intraluminal thrombus (ILT) is found in most of AAAs of clinically relevant size [17,34], and its influence on the wall stress and risk of rupture remains controversial. In vivo [39] and in vitro [22] experimental studies found that the pore pressure in ILT is approximately equal to the blood pressure. Hence, some authors [39] believe that ILT cannot reduce the wall stress. On the other hand, several more recent computational [11,28,36,52] and experimental [42] studies demonstrate the opposite, indicating that ILT has a protective role which depends on the degree of its attachment to the vessel wall [30]. However, while ILT may help to reduce the wall stress, it is also linked with the AAA wall degradation due to oxygen deprivation [14]. Indeed, large thrombi have been associated with faster AAA growth; therefore, the potential for ILT to weaken the AAA wall may be of more critical importance when compared to reduction in the wall stress [34].

The most commonly used predictor of the risk of aneurysmal rupture is the maximum diameter of an aneurysm. However, it has been shown that some large aneurysms do not rupture while some aneurysms with a smaller diameter lose their structural integrity [26,41]. A more reliable predictor of an aneurysm rupture has been shown to be the Peak Wall Stress (PWS) [36,46,52]. A computational model has to be used to compute PWS, and therefore, its value depends on the assumptions made by that model.

M. Bukač (✉)
Department of Applied and Computational Mathematics and Statistics, University of Notre Dame, Notre Dame, IN, USA
E-mail: mbukac@nd.edu

S. C. Shadden
Department of Mechanical Engineering, University of California Berkeley, Berkeley, CA, USA

Published online: 06 September 2021

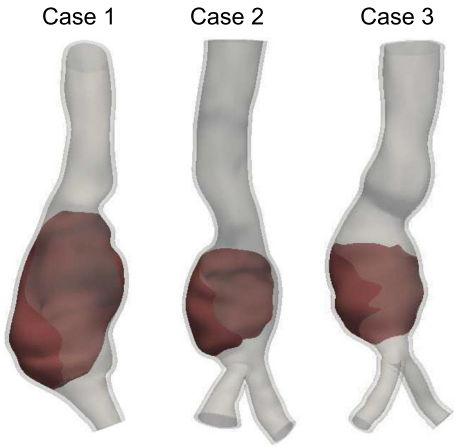


**Fig. 1** The patient-specific geometries used in numerical simulations. The lumen is shown in dark gray, ILT in red and arterial wall in light gray. (Color figure online)

Various constitutive models have been used to include ILT mechanics in computational studies for blood flow in compliant vessels. However, most studies consider the thrombus as a part of the vessel wall, and use similar constitutive models for the thrombus and vessel. For example, linear and nonlinear elastic models, where the ILT region of varying thickness is incorporated into the vessel wall, have been considered by Doyle et al. [11]. Vorp et al. [37,51] developed finite strain constitutive models for both ILT and AAA. These models were used by Wang et al. [52] and Li et al. [28], assuming that both ILT and AAA are hyperelastic, homogenous, incompressible and isotropic materials. Since experimental studies show that thrombi are permeable [49], multiphase and porous media models for ILT have been considered as well. A porohyperelastic description of ILT and the aortic wall has been proposed by Ayyalasomayajula et al. [3] using a coupled porohyperelastic mass transport model. A poroelastic model for ILT has been used by Polzer et al. [36], coupled to an elastic model describing mechanics of the vessel wall. While these studies have shed important insight into thrombus–wall biomechanics, the thrombus–wall interaction has not been coupled to blood flow.

We propose a novel model for the blood flow in AAA with ILT, consisting of a fluid–poroelastic structure interaction problem that captures blood flow in the lumen and within ILT, as well as the deformation of the ILT and vessel wall. The model for ILT, fully coupled with the AAA deformation and blood flow, is based on the Biot's poroelastic equations. The coupling conditions are imposed using the Nitsche's method and the resulting problem is solved using the finite element method in a monolithic fashion, using a specially designed preconditioner. Our simulations are performed in three different patient-specific AAA geometries. Using different ILT permeabilities within a physiological range, we study the effects of ILT on the wall stress in AAA. The effectiveness of our proposed modeling approach is evaluated by comparing our results to the ones obtained using a simplified, purely elastic description of ILT.

## 2 Methods

The numerical simulations are performed in patient-specific geometries shown in Fig. 1.

The lumen is shown in dark gray, ILT in red and arterial wall in light gray. These models were derived from de-identified image data collected for other purposes from 3 patients with AAA that contained thrombus. The vessel lumen and thrombus boundary were segmented using SimVascular [44], which defined the blood flow and ILT domains. The aortic wall was assumed to be of constant thickness (2 mm) and extruded outward from the inner vessel wall defined from the image data. The resulting 3 domains (blood pool, ILT and vessel wall) were volumetrically meshed using tetrahedral elements. The 3 domains, along with their interfaces, were tagged with a unique region IDs. This multidomain mesh was used for finite-element modeling of blood flow and tissue mechanics, as described in the sections below.

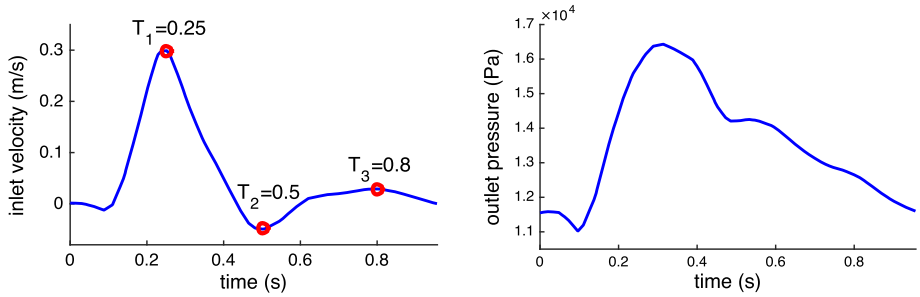


**Fig. 2** Left: The velocity imposed at the inlet of the fluid domain. Red dots denote the phase points of interest used in the Results section, obtained after the periodic regime is established. Right: The pressure imposed at the outlet of the fluid domain. (Color figure online)

### 2.1 Model for blood flow

Blood flow in AAA is mostly laminar or transitional, including during mild exercise [27]. Furthermore, since the abdominal aorta is a large vessel with high shear rates, non-Newtonian effects of blood are small compared to other modeling errors or assumptions [2,24]. Hence, we model blood flow in AAA using the Navier–Stokes equation for an incompressible, viscous fluid, given by

$$\rho_f \left(\partial_t \boldsymbol{v} + \boldsymbol{v} \cdot \nabla \boldsymbol{v}\right) = \nabla \cdot \boldsymbol{\sigma}_{\mathrm{f}}, \tag{1}$$

$$\nabla \cdot \boldsymbol{v} = 0. \tag{2}$$

The fluid velocity is denoted by $\boldsymbol{v}$, the fluid density by $\rho_f$ and the Cauchy stress tensor by $\boldsymbol{\sigma}_{\mathrm{f}} = -p_{\mathrm{f}}\boldsymbol{I} + 2\mu_{\mathrm{f}}\boldsymbol{D}(\boldsymbol{v})$, where $p_{\mathrm{f}}$ is the fluid pressure, $\mu_{\mathrm{f}}$ is the fluid dynamic viscosity, and $\boldsymbol{D}(\boldsymbol{v})$ is the fluid strain rate tensor.

The blood density is taken to be 1000 kg/m$^3$ and viscosity 0.004 Pa s. At the inlet of the fluid domain, we impose pulsatile velocity with uniform profile, with a maximum Reynolds number of 1800 based on vessel diameter. A pressure waveform with a maximum pressure of $1.65 \times 10^4$ Pa ($\sim$123 mmHg) is imposed at the outlet. These values correspond to measurements of aortic velocity and pressure reported by Olufsen et al. [33]. The boundary conditions are shown in Fig. 2.

### 2.2 Model for ILT

To model ILT, we propose a poroelastic model that captures both the flow within ILT and its deformation. In particular, we employ Biot's poroelasticity model [9,10,29], which consists of the equilibrium equation for the balance of total forces, generalized Darcy's law and the continuity equation, respectively, given by

$$\rho_s \partial_t \boldsymbol{V} = \nabla \cdot \left(\boldsymbol{\sigma}_E - \alpha p_{\mathrm{p}} \boldsymbol{I}\right) \tag{3}$$

$$\kappa^{-1}\boldsymbol{q} = -\nabla p_{\mathrm{p}} \tag{4}$$

$$\frac{1}{M}\partial_t p_{\mathrm{p}} + \alpha \nabla \cdot \boldsymbol{V} + \nabla \cdot \boldsymbol{q} = 0, \tag{5}$$

where $\boldsymbol{q}$ is Darcy velocity, $p_{\mathrm{p}}$ is pore pressure, $\boldsymbol{U}$ is displacement, and $\boldsymbol{V} = \partial_t \boldsymbol{U}$ is the solid velocity. The density of the poroelastic material is denoted by $\rho_s$, the permeability is denoted by $\kappa$, and the Biot parameters accounting for compressibility in the two-phase material are $\alpha$ and $M$. We model the solid phase of ILT as an isotropic, linearly elastic structure, whose Cauchy stress tensor, $\boldsymbol{\sigma}_E$, is given by

$$\boldsymbol{\sigma}_E = \frac{E}{1+\sigma}\boldsymbol{D}(\boldsymbol{U}) + \frac{E\sigma}{(1+\sigma)(1-2\sigma)}(\nabla \cdot \boldsymbol{U})\boldsymbol{I}, \tag{6}$$

where $E$ is Young's modulus and $\sigma$ is Poisson's ratio.

We assume that the density of the ILT is 1100 kg/m$^3$ [32,43], the Young's modulus is $1.044 \times 10^5$ Pa, and the Poisson's ratio is 0.45 [11,16]. Furthermore, since ILT is essentially incompressible [36], we take $M = 10^4$ Pa and $\alpha = 1$. Even though some authors assume that ILT is incompressible ($M \to \infty$), we

allow slight compressibility to avoid numerical problems associated with the resulting saddle-point problem. A wide range of permeabilities accounting for inter- and intra-patient variabilities has been reported by Polzer et al. [36]. Following this result, we will use permeabilities in the range $10^{-12} < \kappa < 10^{-8}$ m$^4$ N$^{-1}$ s$^{-1}$.

### 2.3 Model for AAA

Arterial walls are complex structures that consist of several layers with different biomechanical characteristics. Their material properties have been widely studied [21,38]. In applications where arterial wall deformation is coupled to blood flow, common models for arteries include linear and nonlinear elasticity models [15,23,48,50] and viscoelastic models [8,38]. However, even though arteries are characterized by small permeability [19], their poroelastic properties play an important role in the regulation of plasma and solute transport across the wall [55]. Hence, to model an AAA with ILT, we propose to use Biot's poroelasticity model (3)–(5), where different porous and mechanical properties are implemented for the AAA wall and the ILT. We note that the AAA wall does not have significant porous properties. However, adding a poroelastic component to the model does not significantly change the AAA mechanics [55], but it enables us to model the AAA wall and ILT mechanics using a consistent formulation with discontinuous properties. For this purpose, we create a single mesh for the ILT and AAA regions by adding the meshes for AAA and ILT together. System (3)–(5) is solved on that mesh using different material properties in the ILT and AAA regions.

To model the mechanics of AAA, we take Young's modulus to be 9 MPa and a Poisson's ratio of 0.49 [45,54]. The wall density is 1100 kg/m$^3$. Since AAA is nearly incompressible, we assume that the Biot parameters are $M = 10^4$ Pa and $\alpha = 1$. Finally, to account for the low hydraulic conductivity of AAA, we take $\kappa = 10^{-14}$ m$^4$N$^{-1}$s$^{-1}$. The displacement is assumed to be fixed at the inlet and outlet boundaries. At the external boundary, a pressure load acting on the outer surface of the wall is sometimes included to account for the surrounding tissue and organs that affect aortic pulsatility. However, due to the limited published data on the exact magnitude of the abdominal pressure [40], we assume that the aortic wall is exposed to zero external ambient pressure, as often done in the literature [35,53,56].

### 2.4 Coupling of the models of the blood flow, ILT and AAA

Since ILT and AAA are described within a single poroelastic model, to couple them to blood flow we impose the continuity of normal flux, the slip condition with the slip rate $\gamma^{fp}$, the conservation of momentum for the fluid phase and the balance of contact forces [5]:

$$\text{Mass conservation:} \qquad \boldsymbol{v} \cdot \boldsymbol{n}_f = (\boldsymbol{V} + \boldsymbol{q}) \cdot \boldsymbol{n}_f, \tag{7}$$

$$\text{The slip condition:} \qquad \boldsymbol{\tau}_{f,i} \cdot \boldsymbol{\sigma}_f \boldsymbol{n}_f|_{\Gamma^{fp}(t)} = -\gamma^{fp} (\boldsymbol{v} - \boldsymbol{V}) \cdot \boldsymbol{\tau}_{f,i}, \tag{8}$$

$$\text{Momentum conservation:} \qquad \boldsymbol{n}_f \cdot \boldsymbol{\sigma}_f \boldsymbol{n}_f = -p_{\mathrm{p}}, \tag{9}$$

$$\text{Balance of contact forces:} \qquad \boldsymbol{\sigma}_f \boldsymbol{n}_f = (\boldsymbol{\sigma}_E - \alpha p_{\mathrm{p}} \boldsymbol{I}) \boldsymbol{n}_f, \tag{10}$$

where $\boldsymbol{n}_f$ denotes the outward normal to the fluid domain and $\boldsymbol{\tau}_{f,i}$, $i = 1, 2$, denote the corresponding tangential unit vectors. The value of $\gamma^{fp}$ should be determined experimentally. However, since no measurements are available, we present the numerical results using $\gamma^{fp} = 10^3$. Based on results from Bukač and Čanić [6], $\gamma^{fp} = 10^3$ is expected to be sufficiently large to approximate a no-slip condition.

### 2.5 Numerical scheme

Our model for the interaction between blood, ILT and AAA describes a fluid-poroelastic structure interaction problem. To solve this problem numerically, we use the finite element method. In particular, we impose the coupling conditions using Nitche's method in the same way as in our previous work [7]. The submodels are then used to precondition the resulting algebraic problem. This approach has been more fully described and verified on a benchmark problem related to blood flow by Bukač et al. [7], and shown to accelerate the convergence of the GMRES algorithm. Furthermore, this algorithm has been used by Zakerzadeh et al. [55] to simulate blood flow in common carotid arteries. We use the same approach in this work, implemented within a parallel solver MUMPS.

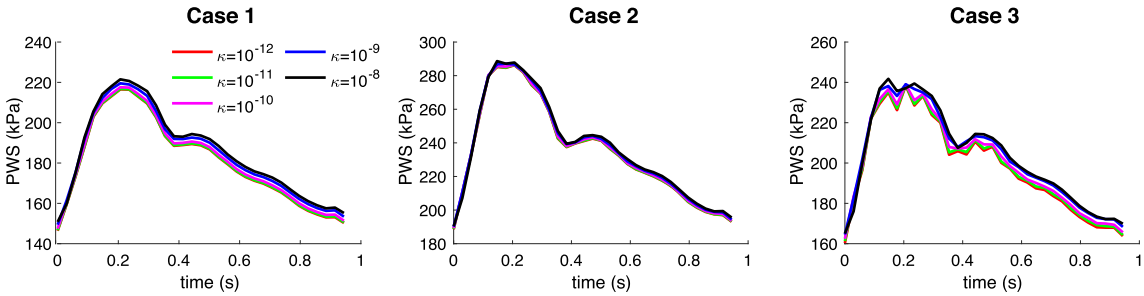


**Fig. 3** PWS for different ILT permeabilities

Mesh convergence study was performed on a steady-state problem, using the mean values of velocity and pressure given in Fig. 2. Computational meshes with increasing number of elements were used until the relative error in PWS was less than 5%. Based on this study, the results presented in the following section were obtained using 188,219 linear tetrahedral elements in the fluid domain and 132,281 linear tetrahedral elements in AAA with ILT in case 1, 273,799 linear tetrahedral elements in the fluid domain and 198,,543 linear tetrahedral elements in AAA with ILT in case 2 and 383,042 linear tetrahedral elements in the fluid domain and 282,336 linear tetrahedral elements in AAA with ILT in case 3. The time step used in the simulations is $10^{-3}$ s. The final results were obtained after 6 cardiac cycles starting from zero initial conditions.

## 3 Results

Numerical simulations of blood flow in AAA with ILT were performed to quantify the relation between ILT permeability and the risk of AAA rupture. To further investigate the role of ILT on AAA wall mechanics, we compare our results to the ones obtained in the same AAA geometry, but without the presence of ILT. Finally, to evaluate the use of a poroelastic description of ILT, we compare our results to the ones obtained with a purely elastic ILT model.

The von Mises stress (VMS) is calculated to quantify wall stress in the AAA and in the ILT. In particular, the risk of wall rupture is manifested by the increase of PWS [36,46], which is defined as the maximum VMS in the AAA wall, given by

$$\text{PWS} = \max\left[\frac{1}{\sqrt{2}}\sqrt{(\sigma_1-\sigma_2)^2+(\sigma_1-\sigma_3)^2+(\sigma_2-\sigma_3)^2}\right], \tag{11}$$

where $\sigma_1$, $\sigma_2$ and $\sigma_3$ are the principal stresses. We compute PWS and other quantities of interest at peak systole ($T_1$), end systole ($T_2$), and mid-diastole ($T_3$), as shown in Fig. 2.

### 3.1 Relation between permeability and PWS

To assess the impact of ILT permeability, we perform numerical simulations using permeabilities $\kappa = 10^{-8}$, $10^{-9}$, $10^{-10}$, $10^{-11}$ and $10^{-12}$ m$^4$ N$^{-1}$ s$^{-1}$, while keeping other parameters unchanged. Figure 3 shows PWS computed in three different AAAs. Our results indicate that varying the permeability of ILT has little to no effect on PWS. We note that the computed values of PWS are similar to the ones previously reported in the literature [13,20,36]. The largest differences are observed in cases 1 and 3; however, the difference between the PWS obtained using the smallest and largest values of $\kappa$ is only about 2%. Although slight, we note that the PWS generally increases as the permeability increases.

### 3.2 Role of ILT on the AAA wall mechanics

To investigate the role of ILT on AAA wall mechanics, we performed numerical simulations in the same geometry, with and without ILT. In both cases, we assume that the AAA wall is poroelastic, described using (3)–(5). The parameters used to represent the AAA wall are described in Sect. 2.3. When ILT is present, we

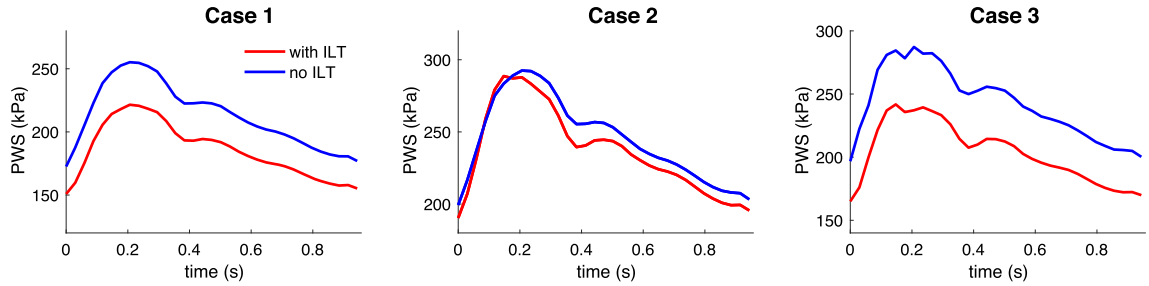


**Fig. 4** Comparison of PWS in AAA not containing ILT (blue line) and AAA containing ILT, modeled as poroelastic material with permeability $\kappa = 10^{-8}$ m$^4$ N$^{-1}$ s$^{-1}$ (red line). (Color figure online)

**Table 1** Peak and mean PWS in the presence and absence of ILT

| Case | Max PWS over the cardiac cycle (kPa) | | Time-average PWS (kPa) | |
|---|---|---|---|---|
| | Without ILT | With ILT | Without ILT | With ILT |
| 1 | 255 | 222 | 213 | 185 |
| 2 | 292 | 289 | 245 | 237 |
| 3 | 287 | 242 | 242 | 203 |

model it as a poroelastic material with permeability $\kappa = 10^{-8}$ m$^4$ N$^{-1}$ s$^{-1}$ [1], using a single mesh for ILT and AAA regions as described in Sect. 2.3. In case when ILT is not present, the ILT mesh is added to the lumen mesh, and the fluid equations are solved in the resulting region.

Figure 4 shows PWS with and without ILT. In all cases, PWS increases when ILT is removed. This was particularly pronounced in cases 1 and 3. Namely, the maximum PWS over the cardiac cycle is 255 kPa in case 1 (287 kPa in case 3) when ILT is not present, while in presence of ILT it decreases to 222 kPa (242 kPa in case 3), see Table 1. The time-average PWS during one cardiac cycle is 213 kPa in case 1 (242 kPa in case 3) in the AAA without ILT and 185 kPa (203 kPa in case 3) in the AAA with ILT. In case 2, the maximum PWS over the cardiac cycle is 289 kPa when ILT is present, and 292 kPa when ILT is not present. The time-average PWS is 237 kPa in the presence of ILT and 245 kPa in the absence of ILT.

To visualize the values of VMS in the interior of the AAA walls, we show bisections obtained in the presence (top) and absence (bottom) of ILT at $T_1$, $T_2$ and $T_3$. Case 1 is shown in Fig. 5, case 2 in Fig. 6 and case 3 in Fig. 7. In case 1, larger values of VMS are observed in the absence of ILT. We also note that the location of occurrence of PWS is different in the presence and the absence of ILT. The PWS in AAA with ILT occurs in the wall region opposite from the ILT, i.e., the posterior side. However, in the absence of ILT, the PWS is located on the anterior side of the AAA. Hence, in case 1 the presence of ILT reduces the PWS in the AAA overall and changes the location of PWS.

In case 2, shown in Fig. 6, the VMS is the largest at the entrance to the AAA and the aortic bifurcation, and it takes similar values in the presence and absence of ILT. However, smaller values of VMS are observed in the anterior side of the wall when ILT is present. We note that in this case AAA and ILT are significantly smaller in size than in case 1.

Figure 7 shows the VMS distribution in case 3. Largest values of VMS are observed in the large curvature region at the neck of the aneurysm, both in presence and absence of ILT. Increased VMS is also seen in the anterior side of the AAA wall when ILT is not present. As in the previous case, AAA and ILT are significantly smaller in size than in case 1.

### 3.3 Comparison of PWS under a nonporous elastic and poroelastic models for ILT

In this section, we investigate the impact of modeling ILT as poroelastic material versus an elastic solid. In the case when ILT is modeled as a poroelastic material, we use permeability $\kappa = 10^{-8}$ m$^4$ N$^{-1}$ s$^{-1}$. When an elastic description is employed for ILT, we extend the model for the AAA wall described in Sect. 2.3 to the ILT region, but choose different material properties for the AAA wall and ILT. In particular, the Young's modulus is 9 MPa for the AAA wall and $1.044 \times 10^5$ Pa for the ILT, while the Poisson's ratio is 0.49 in the

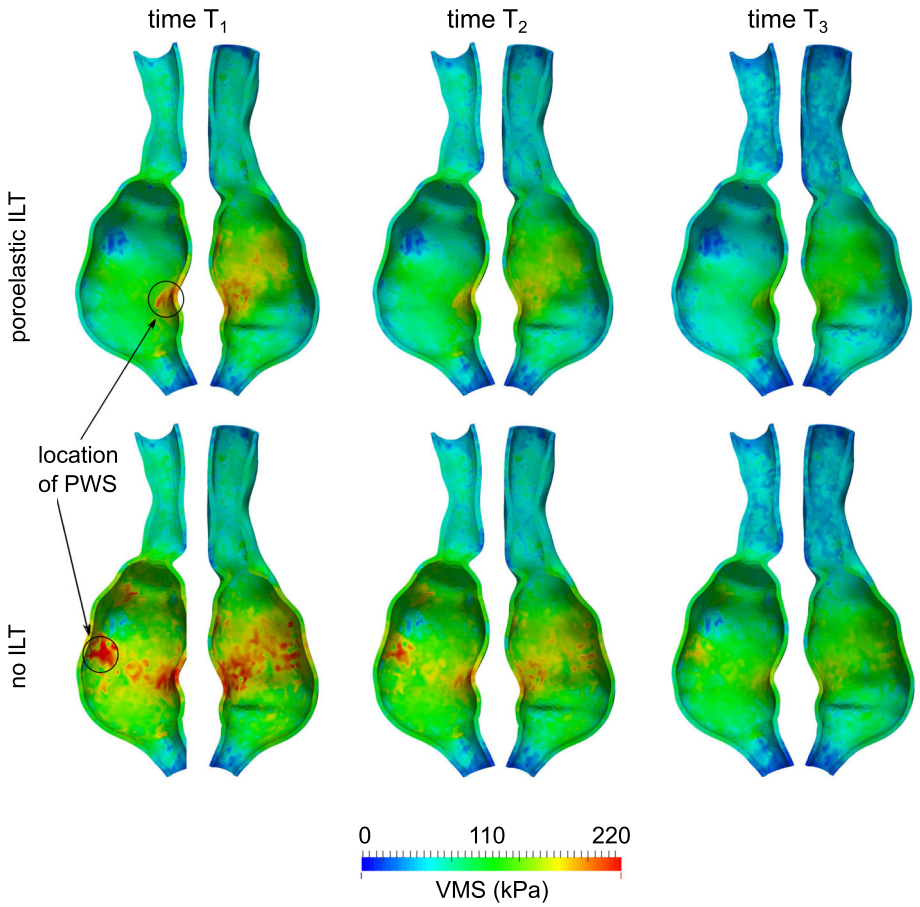


**Fig. 5** The VMS shown in bisected AAA (case 1) obtained when ILT is present (top) and when ILT is absent (bottom) at times $T_1$, $T_2$ and $T_3$. In the case when ILT is present, it is modeled as poroelastic material with permeability $\kappa = 10^{-8}$ m$^4$ N$^{-1}$ s$^{-1}$

AAA and 0.45 in the ILT. We note that the model and material properties for the AAA wall are the same for both elastic and poroelastic ILT.

Figure 8 shows the comparison of the PWS computed using elastic (red line) and poroelastic (blue line) descriptions of ILT in the three cases considered in this study. In all cases, the maximum PWS over the cardiac cycle is similar for porous and nonporous descriptions of ILT. Slightly higher PWS is observed for an elastic ILT in case 1 and case 3, with a difference of 2%.

In contrast to purely elastic models, the poroelastic model captures the fluid velocity in the ILT. Figure 9 shows the velocity magnitude, represented by color and arrow size, and velocity direction, indicated by arrow direction, in three different geometries. The velocity vectors are magnified for visualization purposes. We note that there is a significant inflow into the ILT at peak systole (time $T_1$). At mid-diastole (time $T_3$), the fluid flows from the ILT region into the lumen.

## 4 Discussion

This work investigated the role of ILT on AAA wall mechanics using a poroelastic model of ILT. This model captures both flow inside the ILT and its deformation. The ILT model is fully coupled with blood flow inside the lumen and the vessel wall deformation. Numerical simulations based on the finite element method were performed in three different patient specific AAA geometries under physiological boundary conditions. The ILT model and its parameters were varied to quantify their effects on VMS to gain insight into the role of ILT permeability on potential for aneurysm rupture. The results indicate that the ILT permeability has minimal direct influence on the PWS. Although the differences are small, we observed that less permeable ILTs lower PWS, and thus presumably lower the risk of rupture compared to ILTs with larger permeability.

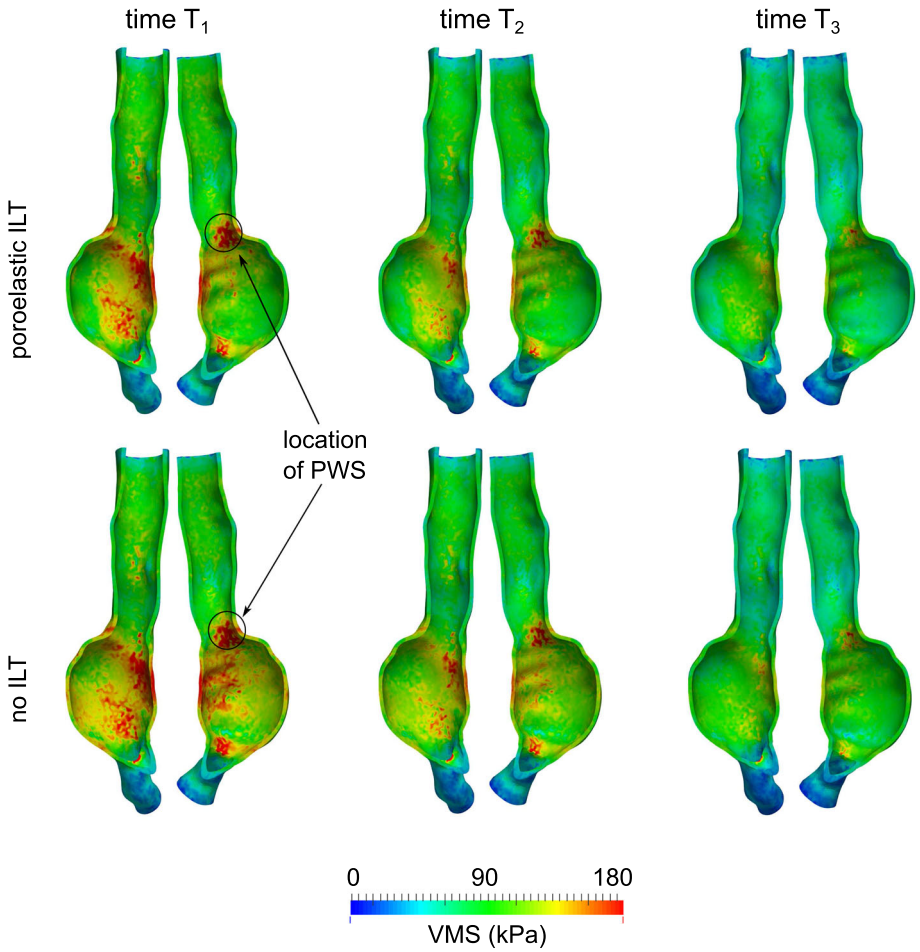


**Fig. 6** The VMS shown in bisected AAA (case 2) obtained when ILT is present (top) and when ILT is absent (bottom) at times $T_1$, $T_2$ and $T_3$. In the case when ILT is present, it is modeled as poroelastic material with permeability $\kappa = 10^{-8}$ m$^4$ N$^{-1}$ s$^{-1}$

We also investigated how the presence of ILT affects PWS and potential for risk of AAA rupture. In regard to case 1, which contained the largest aneurysm and the largest ILT, our results indicated that PWS increases by 15% when ILT is not present. Furthermore, the location where PWS occurred changed dramatically with the ILT "shielding" what would otherwise be the location of PWS. In the presence of ILT, the PWS occurred in the posterior region. In the absence of ILT the same region exhibits elevated stress, however the PWS occurred in the region otherwise covered by ILT. In case 2, the VMS was the largest at the proximal region to AAA and the aortic bifurcation both in the presence and absence of ILT, with similar values in both cases. When the ILT was not present, increased values of VMS were observed in the AAA wall. Finally, in case 3, the PWS occurred in the neck of the AAA, in a region with a large curvature, in the presence and absence of ILT. Slightly increased VMS was observed in the AAA wall when the ILT was not present. Overall, the VMS in the AAA wall was about 18% larger in the absence of ILT. Our results indicate that ILT may reduce the wall stress in AAA and therefore could potentially decrease the risk of wall rupture. However, further studies in a larger number of patient specific geometries are needed to quantify the relation between the AAA size, ILT size and VMS.

Finally, we compared stresses computed using a nonporous elastic and a poroelastic model for ILT. Both models gave similar approximations to the peak PWS in the AAA wall in all three cases. Due to the fluid dissipation present in the model, the poroelastic ILT predicted slightly smaller mean PWS than the elastic ILT model in cases 1 and 3. Hence, a nonporous elastic ILT model may be considered a reasonable model for the purpose of approximating PWS in AAA. However, the porous properties of ILT should be taken into account in studies concerned with biochemical transport, such as modeling of oxygen delivery.

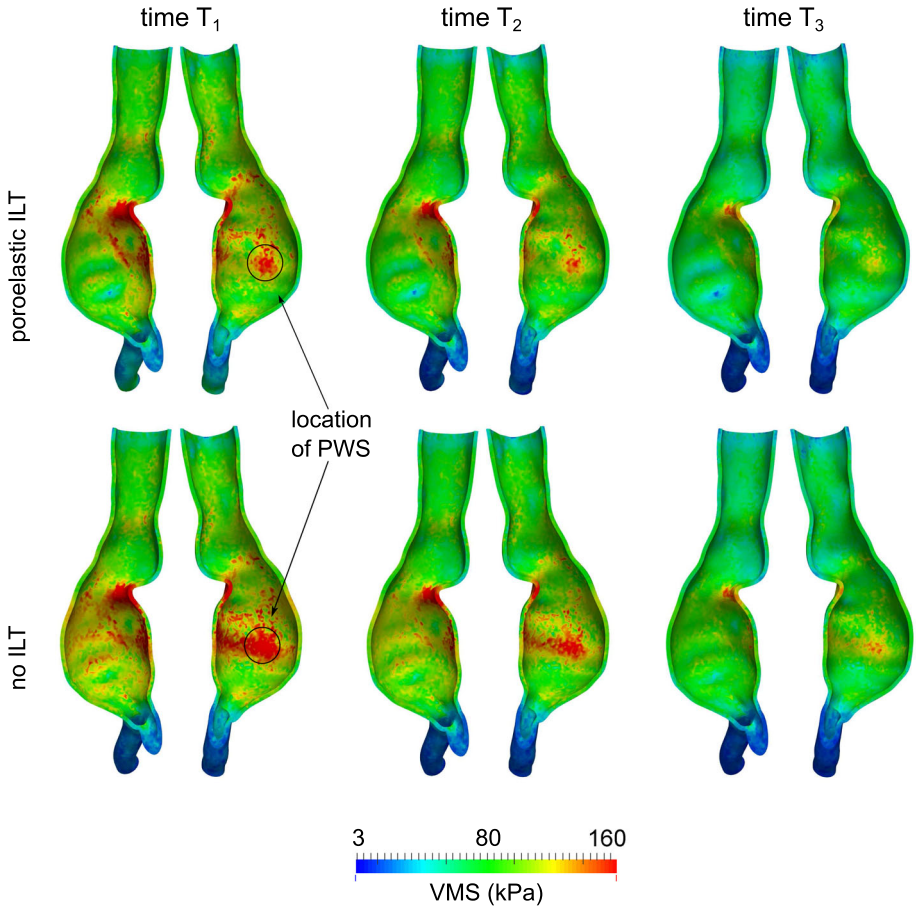


**Fig. 7** The VMS shown in bisected AAA (case 3) obtained when ILT is present (top) and when ILT is absent (bottom) at times $T_1$, $T_2$ and $T_3$. In the case when ILT is present, it is modeled as poroelastic material with permeability $\kappa = 10^{-8}$ m$^4$ N$^{-1}$ s$^{-1}$

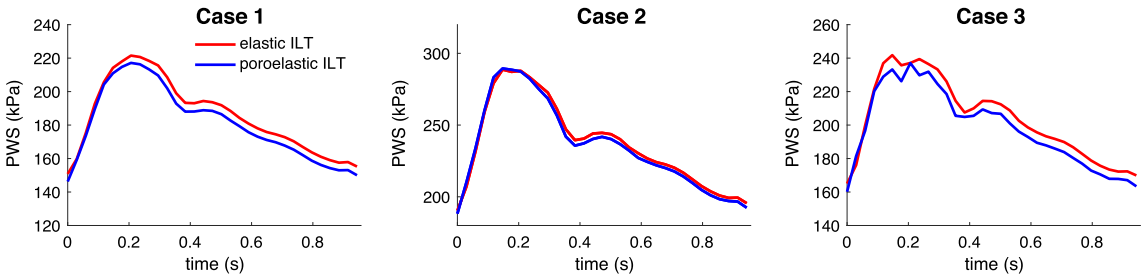


**Fig. 8** Comparison of PWS in AAA obtained using an elastic model for ILT (blue line) and a poroelastic model for ILT with permeability $\kappa = 10^{-8}$ m$^4$ N$^{-1}$ s$^{-1}$ (red line). (Color figure online)

Potential limitations of this study include assuming linear, homogeneous and isotropic constitutive properties for the AAA wall and ILT. Furthermore, a nonzero pressure load acting on the outer surface of the wall should be included in order to obtain a more realistic model. An assumption that the aortic wall is linearly elastic is often used in the literature [4,12,18,25,31,47]. A hyperelastic constitutive model provides a more realistic description of the AAA wall [37], but can be difficult to correctly parameterize and suffers from issues with numerical convergence. Although different material models may lead to different wall stress values, we do not expect the overall conclusions of this study regarding the effect of ILT on PWS to change.

Our future work will consider the implementation of a nonlinear, neo-Hookean model for AAA. Furthermore, we plan to develop more realistic, nonlinear models for ILT that can more accurately represent the ILT microstructure [51]. Since the poroelastic description considered in this study captures the flow in the

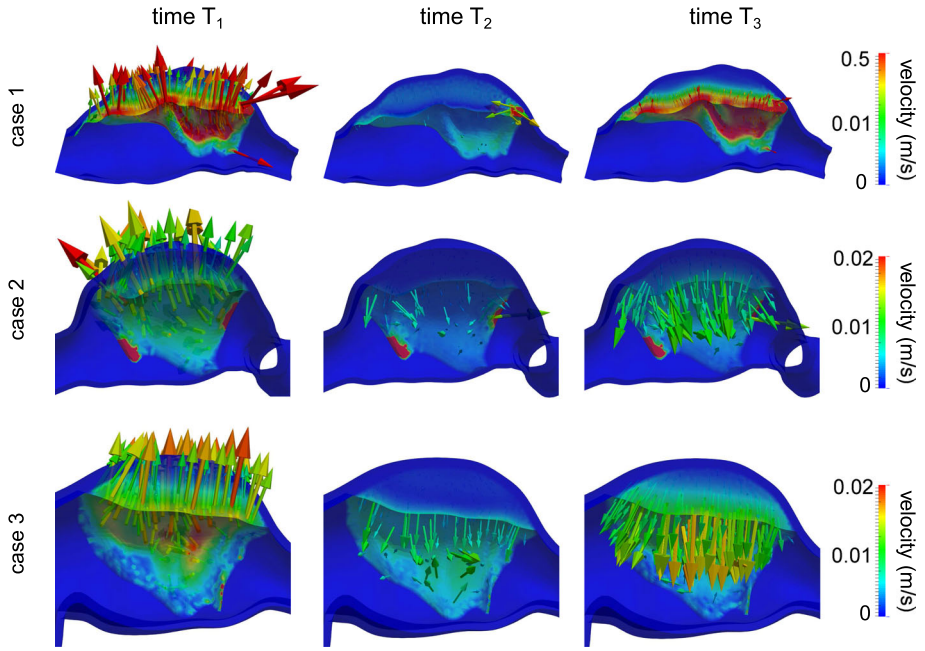


**Fig. 9** The fluid velocity in the ILT at times $T_1$, $T_2$ and $T_3$. Velocity magnitude is represented by color and arrow size. Velocity direction is indicated by arrow direction

ILT, it could be used to model the transport of oxygen to the AAA wall and investigate how thrombus and hemodynamic properties affect the risk of oxygen deprivation.

**Acknowledgements** We would like to thank Miguel A. Rodriguez for his help with the mesh generation. This research of MB is supported by the National Science Foundation (Award Nos. 1912908 and 1934300). SCS acknowledges support from the NSF (Award No. 1354541).

**Declaration**

**Conflict of interest** There is no conflict of interest.

## References

1. Adolph, R., Vorp, D.A., Steed, D.L., Webster, M.W., Kameneva, M.V., Watkins, S.C.: Cellular content and permeability of intraluminal thrombus in abdominal aortic aneurysm. J. Vasc. Surg. **25**(5), 916–926 (1997)
2. Arzani, A.: Accounting for residence-time in blood rheology models: do we really need non-Newtonian blood flow modelling in large arteries? J. R. Soc. Interface **15**(146), 20180486 (2018)
3. Ayyalasomayajula, A., Geest, J., Simon, B.: Porohyperelastic finite element modeling of abdominal aortic aneurysms. J. Biomech. Eng. **132**(10), 104502–104510 (2010)
4. Bazilevs, Y., Gohean, J., Hughes, T., Moser, R., Zhang, Y.: Patient-specific isogeometric fluid-structure interaction analysis of thoracic aortic blood flow due to implantation of the Jarvik 2000 left ventricular assist device. Comput. Methods Appl. Mech. Eng. **198**(45–46), 3534–3550 (2009)
5. Bukač, M.: A loosely-coupled scheme for the interaction between a fluid, elastic structure and poroelastic material. J. Comput. Phys. **313**, 377–399 (2016)
6. Bukač, M., Čanić, S.: A partitioned numerical scheme for fluid–structure interaction with slip. Math. Model. Nat. Phenomena **16**, 8 (2021)
7. Bukač, M., Yotov, I., Zakerzadeh, R., Zunino, P.: Partitioning strategies for the interaction of a fluid with a poroelastic material based on a Nitsche's coupling approach. Comput. Methods Appl. Mech. Eng. **292**, 138–170 (2015)
8. Čanić, S., Tambača, J., Guidoboni, G., Mikelić, A., Hartley, C.J., Rosenstrauch, D.: Modeling viscoelastic behavior of arterial walls and their interaction with pulsatile blood flow. SIAM J. Appl. Math. **67**(1), 164–193 (2006)
9. Chen, J.: Time domain fundamental solution to Biot's complete equations of dynamic poroelasticity. Part II: three-dimensional solution. Int. J. Solids Struct. **31**(2), 169–202 (1994)
10. Debergue, P., Panneton, R., Atalla, N.: Boundary conditions for the weak formulation of the mixed (u, p) poroelasticity problem. J. Acoust. Soc. Am. **106**(5), 2383–2390 (1999)

11. Doyle, B., Callanan, A., McGloughlin, T.: A comparison of modelling techniques for computing wall stress in abdominal aortic aneurysms. BioMed. Eng. Online **6**(38), 137–161 (2007)
12. Figueroa, A., Vignon-Clementel, I., Jansen, K., Hughes, T., Taylor, C.: A coupled momentum method for modeling blood flow in three-dimensional deformable arteries. Comput. Methods Appl. Mech. Eng. **195**(41–43), 5685–5706 (2006)
13. Fillinger, M.F., Raghavan, M.L., Marra, S.P., Cronenwett, J.L., Kennedy, F.E.: In vivo analysis of mechanical wall stress and abdominal aortic aneurysm rupture risk. J. Vasc. Surg. **36**(3), 589–597 (2002)
14. Folkesson, M.: Significance of Intraluminal Thrombus in Abdominal Aortic Aneurysm. Inst för molekylär medicin och kirurgi/Dept of Molecular Medicine and Surgery (2013)
15. Fung, Y.: Elasticity of soft tissues in simple elongation. Am. J. Physiol.-Leg. Content **213**(6), 1532–1544 (1967)
16. Gee, M., Reeps, C., Eckstein, H., Wall, W.: Prestressing in finite deformation abdominal aortic aneurysm simulation. J. Biomech. **42**(11), 1732–1739 (2009)
17. Hans, S., Jareunpoon, O., Balasubramaniam, M., Zelenock, G.: Size and location of thrombus in intact and ruptured abdominal aortic aneurysms. J. Vasc. Surg. **41**(4), 584–588 (2005)
18. Hardy, W.N., Shah, C.S., Kopacz, J.M., Yang, K.H., Van Ee, C.A., Morgan, R., Digges, K.: Study of potential mechanisms of traumatic rupture of the aorta using insitu experiments. Stapp Car Crash J. **50**, 247–266 (2006)
19. Harrison, R.G., Massaro, T.A.: Water flux through porcine aortic tissue due to a hydrostatic pressure gradient. Atherosclerosis **24**(3), 363–367 (1976)
20. Heng, M.S., Fagan, M.J., Collier, J.W., Desai, G., McCollum, P.T., Chetter, I.C.: Peak wall stress measurement in elective and acute abdominal aortic aneurysms. J. Vasc. Surg. **47**(1), 17–22 (2008)
21. Hill, M.R., Duan, X., Gibson, G.A., Watkins, S., Robertson, A.M.: A theoretical and non-destructive experimental approach for direct inclusion of measured collagen orientation and recruitment into mechanical models of the artery wall. J. Biomech. **45**(5), 762–771 (2012)
22. Hinnen, J.-W., Koning, O.H., Visser, M.J., Van Bockel, H.: Effect of intraluminal thrombus on pressure transmission in the abdominal aortic aneurysm. J. Vasc. Surg. **42**(6), 1176–1182 (2005)
23. Humphrey, J.D.: Mechanics of the arterial wall: review and directions. Crit. Rev. Biomed. Eng. **23**(1–2), 1–162 (1994)
24. Khan, M.O., Steinman, D.A., Valen-Sendstad, K.: Non-Newtonian versus numerical rheology: practical impact of shear-thinning on the prediction of stable and unstable flows in intracranial aneurysms. Int. J. Numer. Methods Biomed. Eng. **33**(7), e2836–e2846 (2017)
25. Kim, H.J., Vignon-Clementel, I.E., Figueroa, C.A., LaDisa, J.F., Jansen, K.E., Feinstein, J.A., Taylor, C.A.: On coupling a lumped parameter heart model and a three-dimensional finite element aorta model. Ann. Biomed. Eng. **37**(11), 2153–2169 (2009)
26. Lederle, F., Wilson, S., Johnson, G., Reinke, D., Littooy, F., Acher, C., Ballard, D., Messina, L., Gordon, I., Chute, E., Krupski, W., Busuttil, S., Barone, G., Sparks, S., Graham, L., Rapp, H., Makaroun, M., Moneta, G., Cambria, R., Makhoul, R., Eton, D., Ansel, H., Freischlag, J., Bandyk, D.: Immediate repair compared with surveillance of small abdominal aortic aneurysms. N. Engl. J. Med. **346**(19), 1437–1444 (2002)
27. Les, A.S., Shadden, S.C., Figueroa, C.A., Park, J.M., Tedesco, M.M., Herfkens, R.J., Dalman, R.L., Taylor, C.A.: Quantification of hemodynamicsh in abdominal aortic aneurysms during rest and exercise using magnetic resonance imaging and computational fluid dynamics. Ann. Biomed. Eng. **38**(4), 1288–1313 (2010)
28. Li, Z.-Y., Jean, U., Tang, T., Soh, E., See, T.C., Gillard, J.: Impact of calcification and intraluminal thrombus on the computed wall stresses of abdominal aortic aneurysm. J. Vasc. Surg. **47**(5), 928–935 (2008)
29. Matuszyk, P., Demkowicz, L.: Solution of coupled poroelastic/acoustic/elastic wave propagation problems using automatic hp-adaptivity. Comput. Methods Appl. Mech. Eng. **281**, 54–80 (2014)
30. Meyer, C.A., Guivier-Curien, C., Moore, J.E.: Trans-thrombus blood pressure effects in abdominal aortic aneurysms. J. Biomech. Eng. **132**(7), 071005–1 (2010)
31. Moireau, P., Xiao, N., Astorino, M., Figueroa, A., Chapelle, D., Taylor, C., Gerbeau, J.-F.: External tissue support and fluid-structure simulation in blood flows. Biomech. Model. Mechanobiol. **11**(1–2), 1–18 (2012)
32. Mourad, P.D., Kargl, S.G.: Acoustic properties of fluid-saturated blood clots. Technical report, DTIC Document (2000)
33. Olufsen, M.S., Peskin, C.S., Kim, W.Y., Pedersen, E.M., Nadim, A., Larsen, J.: Numerical simulation and experimental validation of blood flow in arteries with structured-tree outflow conditions. Ann. Biomed. Eng. **28**(11), 1281–1299 (2000)
34. Piechota-Polanczyk, A., Jozkowicz, A., Nowak, W., Eilenberg, W., Neumayer, C., Malinski, T., Huk, I., Brostjan, C.: The abdominal aortic aneurysm and intraluminal thrombus: current concepts of development and treatment. Front. Cardiovasc. Med. **2**, 19 (2015)
35. Polzer, S., Gasser, T.C.: Biomechanical rupture risk assessment of abdominal aortic aneurysms based on a novel probabilistic rupture risk index. J. R. Soc. Interface **12**(113), 20150852 (2015)
36. Polzer, S., Gasser, T., Markert, B., Bursa, J., Skacel, P.: Impact of poroelasticity of intraluminal thrombus on wall stress of abdominal aortic aneurysms. BioMed. Eng. Online **11**, 62–75 (2012)
37. Raghavan, M., Vorp, D.: Toward a biomechanical tool to evaluate rupture potential of abdominal aortic aneurysm: identification of a finite strain constitutive model and evaluation of its applicability. J. Biomech. **33**(4), 475–482 (2000)
38. Robertson, A., Hill, M., Li, D.: Structurally motivated damage models for arterial walls. Theory and application. In: Modeling of Physiological Flows, pp. 143–185. Springer (2012)
39. Schurink, G., Van Baalen, J., Visser, M., Van Bockel, J.: Thrombus within an aortic aneurysm does not reduce pressure on the aneurysmal wall. J. Vasc. Surg. **31**(3), 501–506 (2000)
40. Scotti, C.M., Jimenez, J., Muluk, S.C., Finol, E.A.: Wall stress and flow dynamics in abdominal aortic aneurysms: finite element analysis vs. fluid–structure interaction. Comput. Methods Biomech. Biomed. Eng. **11**(3), 301–322 (2008)
41. The UK Small Aneurysm Trial Participants: Mortality results for randomised controlled trial of early elective surgery or ultrasonographic surveillance for small abdominal aortic aneurysms. Lancet **352**(9141), 1649–1655 (1998)
42. Thubrikar, M., Robicsek, F., Labrosse, M., Chervenkoff, V., Fowler, B.: On abdominal aortic aneurysm wall dilation and stress. J. Cardiovasc. Surg. **44**, 67–77 (2003)

43. Tiari, S., Fatouraee, N., Forouzandeh, F., Mahdavi, M.: Numerical simulation of intraluminal thrombus compliance effects in an abdominal aortic aneurysm using FSI method. In: 2012 19th Iranian Conference of Biomedical Engineering (ICBME), pp. 260–265. IEEE (2012)
44. Updegrove, A., Wilson, N.M., Merkow, J., Lan, H., Marsden, A.L., Shadden, S.C.: Simvascular: an open source pipeline for cardiovascular simulation. Ann. Biomed. Eng. **45**(3), 525–541 (2017)
45. Veer, M., Buth, J., Merkx, M., Tonino, P., van den Bosch, H., Pijls, N., van de Vosse, F.: Biomechanical properties of abdominal aortic aneurysms assessed by simultaneously measured pressure and volume changes in humans. J. Vasc. Surg. **48**(6), 1401–1407 (2008)
46. Venkatasubramaniam, A., Fagan, M., Mehta, T., Mylankal, K., Ray, B., Kuhan, G., Chetter, I., McCollum, P.: A comparative study of aortic wall stress using finite element analysis for ruptured and non-ruptured abdominal aortic aneurysms. Eur. J. Vasc. Endovasc. Surg. **28**(2), 168–176 (2004)
47. Vignon-Clementel, E.: A coupled multidomain method for computational modeling of blood flow. Ph.D. thesis, Mechanical Engineering Department, Stanford University, California, USA (2006)
48. Vito, R., Dixon, S.: Blood vessel constitutive models-1995–2002. Annu. Rev. Biomed. Eng. **5**(1), 413–439 (2003)
49. Vorp, A., Steed, D., Webster, D., Kameneva, M., Watkins, S.: Cellular content and permeability of intraluminal thrombus in abdominal aortic aneurysm. J. Vasc. Surg. **25**(5), 916–926 (1997)
50. Vorp, D.A., Rajagopal, K., Smolinski, P.J., Borovetz, H.S.: Identification of elastic properties of homogeneous, orthotropic vascular segments in distension. J. Biomech. **28**(5), 501–512 (1995)
51. Wang, D., Makaroun, M., Webster, M., Vorp, D.: Mechanical properties and microstructure of intraluminal thrombus from abdominal aortic aneurysm. J. Biomech. Eng. **123**(6), 536–539 (2001)
52. Wang, D., Makaroun, M., Webster, M., Vorp, D.: Effect of intraluminal thrombus on wall stress in patient-specific models of abdominal aortic aneurysm. J. Vasc. Surg. **36**(3), 598–604 (2002)
53. Wolters, B., Rutten, M., Schurink, G., Kose, U., De Hart, J., Van De Vosse, F.: A patient-specific computational model of fluid-structure interaction in abdominal aortic aneurysms. Med. Eng. Phys. **27**(10), 871–883 (2005)
54. Xiong, J., Wang, S.M., Zhou, W., Wu, J.G.: Measurement and analysis of ultimate mechanical properties, stress–strain curve fit, and elastic modulus formula of human abdominal aortic aneurysm and nonaneurysmal abdominal aorta. J. Vasc. Surg. **48**(1), 189–195 (2008)
55. Zakerzadeh, R., Bukac, M., Zunino, P.: Computational analysis of energy distribution of coupled blood flow and arterial deformation. International Journal of Advances in Engineering Sciences and Applied Mathematics **8**(1), 70–85 (2016)
56. Zelaya, J.E., Goenezen, S., Dargon, P.T., Azarbal, A.-F., Rugonyi, S.: Improving the efficiency of abdominal aortic aneurysm wall stress computations. PLoS ONE **9**(7), e101353 (2014)